A Novel Scaffold-Reinforced Actuator With Tunable Attitude Ability for Grasping

Pei Jiang, *Member, IEEE*, Ji Luo, Jiaxing Li, Michael Z. Q. Chen, *Senior Member, IEEE*, Yonghua Chen, *Member, IEEE*, Yang Yang, *Member, IEEE*, and Rui Chen

***Abstract*—Owing to high compliance, adaptiveness, and easy controllability, soft actuators are widely adopted in soft grippers to grasp irregularly shaped or fragile objects. The specific motions can be preprogrammed into the flexible and constrained structures of the actuator, which provides an inexpensive and convenient method for desired motions. However, most preprogrammed structures cannot change the constraints on the actuator to achieve different kinds of deformations, which limits the motion diversities of actuators. This article proposes a scaffold reinforcement mechanism, where rotatable scaffolds distribute on the surface of the soft structure. The orientation adjustments of the scaffolds can change the deformation constraint of the actuator, which results in different kinds of motions. Based on the scaffold reinforcement mechanism, a scaffold-reinforced actuator is proposed, which can achieve bending motion and complex helical motion in the 3-D space by properly adjusting the orientation of the scaffolds. In addition, both the kinematic and mechanical models are proposed to forecast the behavior of the actuator when driven by cable displacement or tension force. Experimental results verify the validity of the theoretical model, and the actuator can achieve an independent control of bending and helical motion, which can be adopted in applications where both high dexterity and flexibility are required.**

***Index Terms*—Cable driven, helical motion, scaffold reinforcement, soft actuator, soft gripper.**

Manuscript received 7 March 2022; revised 12 July 2022; accepted 10 August 2022. This article was recommended for publication by Associate Editor R. Kramer-Bottiglio and Editor A. Menciassi upon evaluation of the reviewers' comments. This work was supported in part by the National Natural Science Foundation of China under Grant 51705050, Grant 52005269, and Grant 52075060, in part by the Key Project of Science and Technology Research Program of Chongqing Education Commission of China under Grant KJZD-K201901105, and in part by the Fundamental Research Funds for the Central Universities under Grant 2022CDJKYJH024. *(Corresponding authors: Pei Jiang; Michael Z. Q. Chen.)*

Pei Jiang, Ji Luo, and Rui Chen are with the State Key Laboratory of Mechanical Transmission, University of Chongqing, Chongqing 400030, China (e-mail: peijiang@cqu.edu.cn; jiluo@cqu.edu.cn; cr@cqu.edu.cn).

Jiaxing Li was with the State Key Laboratory of Mechanical Transmission, University of Chongqing, Chongqing 400030, China. He is now with TD Technology Co. Ltd., Chengdu 610041, China (e-mail: lijiaxing_cqu@qq.com).

Michael Z. Q. Chen is with the School of Automation, Nanjing University of Science and Technology, Nanjing 210094, China (e-mail: mzqchen@outlook.com).

Yonghua Chen is with the Department of Mechanical Engineering, University of Hong Kong, Pokfulam, Hong Kong (e-mail: yhchen@hku.hk).

Yang Yang is with the School of Automation, Nanjing University of Information Science and Technology, Nanjing 210044, China (e-mail: meyang@connect.hku.hk).

This article has supplementary material provided by the authors and color versions of one or more figures available at https://doi.org/10.1109/TRO.2022.3200550.

Digital Object Identifier 10.1109/TRO.2022.3200550

I. Introduction

COMPARED with traditional rigid-body robots, soft robots can achieve high compliance, adaptability, and safety by preprogramming complex motions into flexible structures and showing their outstanding advantages in grasping soft objects with irregular shapes, adaptability to unknown environments, and convenient control, which have attracted more and more research interest in recent years. Diverse stimuli, such as fluidic pressures (pneumatic or hydraulics) [1], [2], [3], [4], [5], [6], [7], [8], [9], [10], [11], tendons [12], [13], [14], [15], electric/magnetic forces [16], [17], [18], [19], [20], and chemical reactions [21] are adopted to trigger soft actuators. Hence, transforming the power into the deformation of the soft robot by preprogramming the desired motions into the soft structure becomes a popular research topic.

The pneumatic artificial muscle (PAM) appeared as an early actuator in the 1950s, which is featured with the axial extension/contraction, and bending under pressurization and has been widely applied in computer–human interaction scenarios. A class of pneumatic networks (PneuNets) bending actuators was developed in [22] and [23], which can conduct bending behavior due to the material inconsistency of the embedded chambers when being pressurized. Nevertheless, the tubular chamber structure of the PneuNets bending actuator complicates the actuator design process. The fiber-reinforced bending actuator was proposed in [24] and [25], whose fiber reinforcement winding in a double-helix pattern constrains the radical deformation of the actuator and a strain-limiting layer embedded inside the actuator produces the bending behavior of the actuator in the corresponding direction. In addition, a particle jamming mechanism was introduced to adjust the stiffness of the fiber-reinforced bending actuator [26], [27], [28], [29], [30]. Yang et al. [31] combined soft pneumatic actuation and muscle-like supercoiled polymer actuation to achieve bending motions and variable stiffness. However, these actuators can only achieve motion in a 2-D plane rather than the 3-D space [32]. This behavior may lead to two drawbacks: 1) the reachable workspace of the 2-D bending actuators is limited; and 2) these kinds of actuators cannot achieve dexterous motions in the 3-D space.

Fortunately, helical motions are ubiquitous (e.g., octopus arms for grasping/tendrils for climbing and elephant trunks for grasping) and widely explored due to their dexterity, flexibility, and gripping power. Inspired by these attractive characteristics, many soft actuators with helical deformation emerged. Guan

et al. [33] proposed a family of helical extensile PAMs/helical contractile PAMs exploiting reinforced flexible frames in different orientations, which show the gripping and posing capabilities in the 3-D space. The soft PneuNet actuators were proposed to achieve the helical motion by preprogramming the desired deformation into an oblique chamber structure [34], [35], [36], [37], [38], [39]. The fiber-reinforced actuator can also achieve helical motion with single-helix pattern fiber reinforcement attributing to its expansion along the direction of the fiber when pressurized [40].

In addition, Santoso et al. [41] utilized variable stiffness material to achieve multiple-degree-of-freedom actuation. Tonazzini et al. [42] used patterned variable stiffness fibers to control a continuum actuator in the 3-D space. Nevertheless, the response of these actuators under thermal stimuli is quite slow. Wang et al. [43] proposed a helical actuator based on polymer–paper bilayer composite. The polymer, which can respond to external stimuli, is fabricated by 3-D printing on a paper substrate with twill patterns. Owing to the constraint of the paper substrate, the actuator can achieve a helical motion when the polymer–paper bilayer composite is actuated by external stimuli. Based on the deformation principle, a shape-memory-alloy-based 3-D printed helical actuator, which is composed of a soft matrix with rigid fibers diagonally printed on its bottom surface, was proposed in [44]. However, the variations of helical pitch and radius are determined once the structure parameters of these helical actuators based on the polymer–paper bilayer composite are designed, which cannot change in the application.

The constrained structures, in general, such as fiber reinforcement and twill pattern polymer, are embedded into the actuator to achieve specific motions, which are important in the soft robot field as a means of tailored specific deformation. However, these actuators cannot change their shapes or posture due to their immobilization of the structure. As a result, these actuators cannot conduct the other motions except the preprogrammed ones, which limits the motion diversity. Reconfigurable structures are adopted to achieve motion diversity. Yoshida et al. [45] proposed an actuator, which can implement different behavior (e.g., twist, elongate, and contract) via changing the fiber alignment. However, the 2-D workspace of the actuator is not large enough to realize more sophisticated tasks. Moreover, Kim et al. [46] utilized reconfiguring inflation trajectories of 2-D and 3-D spaces by adhering lamina to the surface of their actuators to achieve more complicated tasks. Nevertheless, it is hard to accurately adhere the lamina to the initial 3-D shape of soft bodies.

In view of the above limitations, a scaffold-reinforced actuator is proposed, as shown in Fig. 1. Herein, a dual-layer structure is adopted, which is composed of a soft layer and a scaffold reinforcement layer. The scaffold reinforcement layer is featured with rotatable scaffolds distributed on the surface of the soft structure. It should be noted that the stiffness of the scaffold is higher than that of the soft layer. Thus, the actuator can only bend around an axis parallel to the scaffold and curl up to a helix in the 3-D space when actuated. Moreover, there does not exist any force between the two layers when the structure is in its natural state. Consequently, the direction of the scaffolds can be adjusted

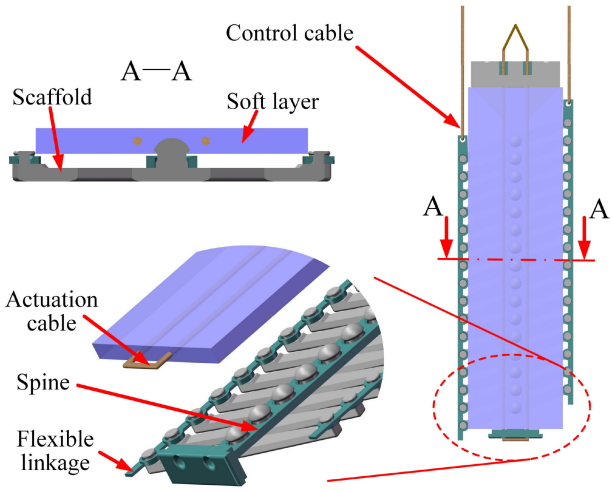

Fig. 1. Structure of the proposed actuator based on scaffold reinforcement.

dynamically to achieve different helical postures. In contrast to the traditional method, the scaffold-reinforced actuator can implement the decoupled control of helical radius and pitch.

Importantly, the main contributions of this article are as follows.

1) A scaffold-reinforced mechanism is proposed as an effective and convenient way to achieve different 3-D motions by adjusting the cable-driven scaffold constraint, which has not yet been reported in the literature.
2) A dual-layer structure is proposed based on the scaffold-reinforced mechanism, which can independently control the helical radius and the pitch of the helical motion simultaneously by adjusting the orientation of the scaffolds.
3) Theoretical models are presented to quantitatively analyze the behavior of the actuator when driven by the displacement or the tension of the actuation cable.

The rest of this article is organized as follows. Section II demonstrates the basic structure of the scaffold-reinforced actuator and the corresponding deformation principle. Then, a kinematic model is presented to analyze the helical motion in Section III, where a mechanical model is also developed based on energy theory. Section IV presents the fabrication process of the actuator based on the scaffold reinforcement method. The experimental results verify the validity of the theoretical models in Section V. Finally, Section VI concludes this article with some brief discussion.

II. Innovative Actuator Design

A. Actuator Design

Fig. 1 depicts the basic designs of the proposed scaffold-reinforced actuator based on a dual-layer structure. The actuator consists of a soft layer and a scaffold reinforcement layer. The former is fabricated by elastic material to endow the actuator with sufficient flexibility, and an actuation cable is also inserted into the U-tube embedded in the soft layer. The latter is composed of uniformly distributed rigid scaffolds, a flexible spine, and flexible linkages. The scaffolds support the

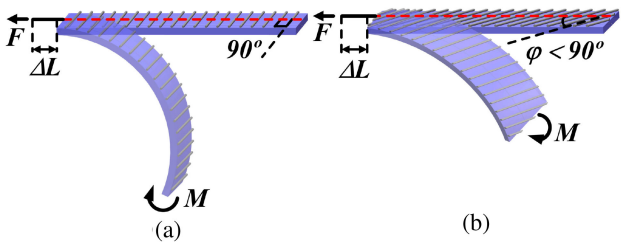

Fig. 2. Concept of scaffold reinforcement element. (a) Bending motion when scaffolds are perpendicular to the spine. (b) Helical motion when scaffolds are not perpendicular to the spine.

soft layer because of their higher stiffness, which can enhance the stiffness of the actuator. Furthermore, the scaffold can constrain the bending direction of the actuator. Because of the hinge connections, the adjacent scaffolds, spine, and flexible linkages form a parallelogram structure, which ensures the consistency of the deflection angles between the scaffolds and the spine. Two control cables connect to the two flexible linkages, respectively, to control the deflection angle between the scaffolds and the spine. The two layers are combined as a unit by the ball joints embedded in the middle of the scaffolds.

B. Deformation Principle

Compared with the pure bending actuators, the scaffold reinforcement endows the actuator with more deformation diversity. In the free state, the actuation cable is slack, the actuator keeps the original shape, and there does not exist pressure between the two layers. Therefore, the scaffolds can rotate freely, and the orientation of the scaffolds can be regulated by properly adjusting the control cables.

When the actuator is driven, the case of the scaffolds perpendicular to the spine is considered first. Once the actuation cable is driven, the change of the cable displacement leads to the tension increase. Thus, a force is generated on the tip of the distal end along the actuation cable, which results in a bending moment toward the soft layer due to the offset between the actuation cable and the neutral layer, as shown in Fig. 2. Note that the pressure and the friction force between the two layers would maintain the direction of the scaffolds relative to the spine during the deformation process.

If the scaffolds are not perpendicular to the spine, the strain-limiting along one direction of the actuator depends on the scaffolds' angle due to the scaffolds' stiffness being much larger than that of the linear elastic material used in the soft layer. Moreover, the component of the driven force perpendicular to the scaffold still leads to a moment toward the soft layer. Since the component force is not perpendicular to the spine, the bending axis of the actuator is not parallel to the scaffold. Therefore, the actuator curls up to an approximate helix, considered as coupled bending and twisting motions in the 3-D space, as shown in Fig. 2. Therefore, the deflection angle can determine the degree of the twist. Similarly, the deflection angle would remain constant during the deformation due to the pressure and the friction force between the two layers.

III. Modeling

A. Assumptions

According to the deformation principle, the actuator deformation is determined on the condition that the helical radius and pitch are determined. Before analyzing the deformation of the actuator, some assumptions are made as follows.

1) The scaffold reinforcement layer is continuous, and the soft layer and the scaffold reinforcement layer connect tightly.
2) There does not exist friction between the control cable and the silicone layer.
3) The actuator generates constant curvature deformation all the time during the deformation process.
4) The deflection angle remains constant during the deformation process.
5) The silicone material is an isotropic linear elastic material.
6) The kinematic model neglects curvature in the direction perpendicular to the spine.
7) The elastic energy stored in the actuation cable is negligible.

B. Kinematic Model

The proposed actuator can achieve desired helical deformation by properly controlling the actuation cable displacement. Furthermore, the geometrical parameters also affect the behavior of the proposed actuator. Therefore, the influences of the geometrical parameters of the actuator and the actuation cable displacement are quantitatively analyzed.

Provided that the assumptions 1), 3), and 4) are satisfied during the actuator deformation process, a kinematic model can be developed based on the geometrical relationship of the helix. Denote the helical pitch, helical radius, helical angle, and deflection angle between the spine and the scaffold as P, R, θ, and φ, respectively, as shown in Fig. 3. To describe the geometrical relation between θ and φ unfolded drawing, a plane coordinate is defined on the unfolded drawing of the actuator, whose X-axis and Y-axis are along the vertical direction of the scaffold and the axial of the helix, respectively, as shown in Fig. 3(c). According to the deformation principle, the scaffolds are always parallel to the axis of the helix, and the spine is along the helical curve; thereby, the following equation can be obtained based on the unfolded drawings of the actuator:

$$\varphi + \theta = \frac{\pi}{2}. \tag{1}$$

Since the deflection angle φ does not change during the helical deformation, the helical angle θ remains a constant once the initial value of φ is determined before actuation. The helical radius is the only factor determining the state of helical motion on the condition that the design parameters and deflection angle are given. Therefore, it is essential to depict the relationship between the helical radius and the actuation variable.

The modulus of elasticity of the spine is much larger than that of the soft layer, assuming that the length of the spine does not change during the helical deformation. Denote the length of the

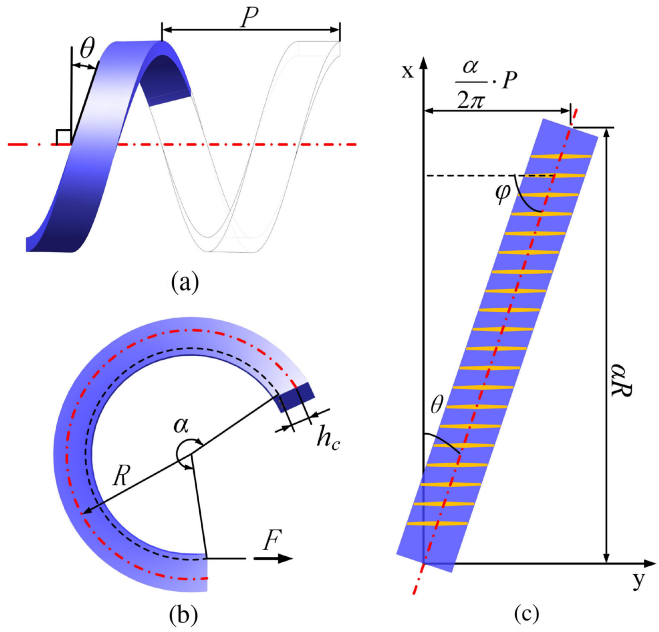

Fig. 3. Kinematic analysis of the proposed actuator. (a) Front view. (b) Side view; the dashed-dotted line represents the spine, and the dashed line represents the actuation cable. (c) Unfolded drawing; the solid lines represent the scaffolds, and the dashed-dotted line represents the spine.

spine and the bending angle as L and α, respectively. According to Fig. 3, the following equation can be obtained:

$$\alpha \cdot R = L \cos\theta. \tag{2}$$

During the helical deformation, the actuation cable displacement decreases. Accordingly, the soft layer is compressed due to the driven force. Assume that the offset between the actuation cable and the spine does not change during the deformation. The offset between the actuation cable and the spine is denoted as h_c, as shown in Fig. 3(b), and the actuation cable displacement is defined as ΔL_a. These assumptions lead to the following equation:

$$\alpha \cdot (R - h_c) = (L - \Delta L_a)\cos\theta. \tag{3}$$

Dividing (2) by (3), one has

$$\frac{R}{R - h_c} = \frac{L}{L - \Delta L_a} \tag{4}$$

which can be simplified as

$$R = \frac{h_c}{\Delta L_a} L. \tag{5}$$

For a cycle of the helix, one has

$$\tan\theta = \frac{P}{2\pi R}. \tag{6}$$

Substituting (1) and (5) into (6), we obtain

$$P = 2\pi R \cdot \tan\theta = \frac{2\pi h_c L}{\Delta L_a} \cdot \tan\left(\frac{\pi}{2} - \varphi\right). \tag{7}$$

Since h_c and L are the design parameters of the actuator, φ can be adjusted by the control cables in a free state. According to (5) and (7), P and R are inversely proportional to ΔL_a. Therefore, a large value of ΔL_a makes the actuator deform more significantly, while the helical radius and pitch become smaller with a large value of ΔL_a. Furthermore, the helical pitch has a negative correlation with the deflection angle. Namely, a larger value of the deflection angle directly diminishes the twisting effect. Especially, if the scaffolds are perpendicular to the spine, the helical pitch is 0, and the corresponding helical deformation becomes a pure bending. Since the deflection angle φ is only related to the pitch P, it provides the possibility for the decoupling control of the helical radius and pitch. According to the twisting requirement, the deflection angle can be modified at first by adequately adjusting the length of the control cable in a free state, and then, the actuation cable can be controlled to achieve desired helical motion.

C. Mechanical Model

In Section III-B, the kinematic model analyzes the behavior of the proposed actuator based on the geometrical relations. However, it does not consider the influences of the characters of the actuator material and cannot forecast the behavior of the actuator under certain cable tension. Therefore, a mechanical model is proposed in this part.

The minimum potential energy method [47] is adopted to forecast the deformation of the proposed actuator. Provided that the assumptions 1)–4) hold, based on [37] and [48], a total potential energy function $\prod$ is denoted as

$$\prod = U_e + W_c \tag{8}$$

where U_e and W_c represent the elastic potential energy stored in the dual-layer structure and input energy, respectively. The elastic potential energy magnitude of the dual-layer structure can be calculated based on two second-order strain matrices, which is formulated as

$$U_e = \sum_{i=1}^{2} \int \frac{1}{2} \boldsymbol{\varepsilon}^{(i)} : \boldsymbol{C}^{(i)} : \boldsymbol{\varepsilon}^{(i)} dv_i \tag{9}$$

where $i \in \{1, 2\}$; it represents the layer of the actuator. For $i = 1$, it represents the soft layer of the actuator with thickness h_1, while for $i = 2$, it represents the scaffold reinforcement layer with thickness h_2, as shown in Fig. 4(b). Variable v_i is a finite element of the volume in the ith layer. Variable $\boldsymbol{\varepsilon}^{(i)}$ represents the second-order strain matrices, and $\boldsymbol{C}^{(i)}$ represents the fourth-order material stiffness matrices. Symbol : represents the two-point product of matrices [49], and the elastic potential energy of each layer obtained by (9) is scalar. Hence, the total elastic potential energy of the dual-layer structure can be obtained by summing up the integration of the elastic potential of infinitesimal elements in each layer. For the potential energy of each layer, the fourth-order material stiffness matrix $\boldsymbol{C}^{(i)}$ conforms to the principle of symmetry; therefore, it can accomplish the mathematical operation with the strain matrix $\boldsymbol{\varepsilon}^{(i)}$.

The input energy can be formulated as

$$W_c = F_c \cdot \Delta L_a \tag{10}$$

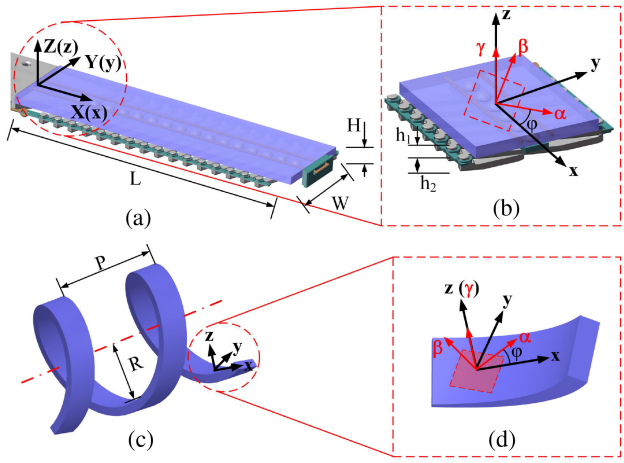

Fig. 4. Detailed parameters and coordinate systems of the actuator. (a) Cartesian coordinate frame. (b) Diagram of the partial actuator, which is consisted of a silicon layer with thickness h_1 and a scaffold-reinforced layer with thickness h_2. (c) Demonstration of a helical deformation schematic diagram. (d) Principal strain plane α–β, where the α-axis rotates anticlockwise from the x-axis by φ.

where F_c is a scalar, which represents the tension of the actuation cable. ΔL_a is defined same as before.

To describe the deformation of the proposed actuator, several coordinates are defined. First, a global coordinate frame X–Y–Z is introduced, whose origin point is at the base of the actuator. X-axis, Y-axis, and Z-axis always orient along with the length, width, and thickness of the actuator, respectively, as shown in Fig. 4(a). Then, a local relative reference coordinate frame x–y–z is introduced, whose origin point of the frame is at the center of the upper surface of the soft layer and the directions of the frame are parallel to the global coordinate frame in the original free state, as shown in Fig. 4(b). Nevertheless, the direction of the local relative reference frame will be changed as the actuator deforms. Finally, a scaffold-based relative reference coordinate frame α–β–γ is introduced to describe the relative deformation between the two layers. α-axis can be obtained by rotating the x-axis around the z-axis with scaffold deflection angle φ; γ is along the direction of the z-axis of the local relative reference coordinate frame.

Based on the Euler–Bernoulli beam theory in material mechanics [47], shear deformation can be neglected during the deformation process for a long straight beam. Therefore, there does not exist shear deformation in the finite-element volume on the strain plane α–β, and the strain tensor only has three positive components. Denote the strain tensor in any plane parallel to the plane α–β as $\boldsymbol{\varepsilon}^r$, which can be formulated in the α–β–γ frame

$$\boldsymbol{\varepsilon}^r = \varepsilon_{11}^r \boldsymbol{\alpha} \otimes \boldsymbol{\alpha} + \varepsilon_{22}^r \boldsymbol{\beta} \otimes \boldsymbol{\beta} + \varepsilon_{33}^r \boldsymbol{\gamma} \otimes \boldsymbol{\gamma} \tag{11}$$

where $\boldsymbol{\alpha}, \boldsymbol{\beta}$, and $\boldsymbol{\gamma}$ represent three orthogonal direction vectors. ε_{11}^r, ε_{22}^r, and ε_{33}^r represent three principal components of the strain in the α–β–γ frame, respectively. $\varepsilon_{11}^r = e_{11} + z\kappa_1$, $\varepsilon_{22}^r = e_{22} + z\kappa_2$, and $\varepsilon_{33}^r = e_{33} + zq$, z denotes the distance between any parallel plane and the α–β principal plane, the variable q denotes the gradient of the strain component along the z-axis, and κ_1 and κ_2 are the curvature along the α and β axes, respectively. e_{11}, e_{22}, and e_{33} represent three principal components of strain tensor at $z = 0$ plane in the α–β–γ frame, respectively.

For the soft layer, the corresponding strain matrix is set in the local relative reference coordinate frame x–y–z for computation convenience. The corresponding strain matrix in the scaffold-based relative reference coordinate frame α–β–γ can be mapped into the local relative reference coordinate frame x–y–z; therefore, the corresponding transformation matrix $\boldsymbol{Q}^{(1)}$ can be defined as

$$\boldsymbol{Q}^{(1)} = \begin{bmatrix} \sin\varphi & \cos\varphi & 0 \\ -\cos\varphi & \sin\varphi & 0 \\ 0 & 0 & 1 \end{bmatrix} \tag{12}$$

where φ is a nonzero value in the transformation matrix.

According to the coordinate transformation formula, the corresponding strain tensor in the x–y–z frame can be obtained as

$$\boldsymbol{\varepsilon}^{(1)} = \boldsymbol{Q}^{(1)^T} \boldsymbol{\varepsilon}^r \boldsymbol{Q}^{(1)}. \tag{13}$$

For the scaffold reinforcement layer of the actuator, the scaffolds restrict the direction of the helical deformation of the actuator, namely, the scaffolds parallel to the direction of the central line of helical deformation. Based on the Euler–Bernoulli beam theory, the corresponding strain matrix should be set in the scaffold-based relative reference coordinate frame α–β–γ. Hence, the strain tensor in the scaffold-based relative reference coordinate frame α–β–γ can be directly obtained as

$$\boldsymbol{\varepsilon}^{(2)} = \boldsymbol{\varepsilon}^r. \tag{14}$$

Both the scaffold reinforcement and soft layers of the actuator are made of linear elastic materials. The fourth-order stiffness matrix can be formulated in the material Young modulus E_m and the Poisson ratio μ_m. Based on the Voigt symmetry principle [50], the stiffness matrices of different materials can be simplified into an explicit formulation. The first layer of the actuator is made of silicone, which is an isotropic linear elastic

$$\left[C^{(1)}\right] = \frac{E_m}{(1+\mu_m)(1-2\mu_m)} \begin{bmatrix} 1-\mu_m & \mu_m & \mu_m & 0 & 0 & 0 \\ \mu_m & 1-\mu_m & \mu_m & 0 & 0 & 0 \\ \mu_m & \mu_m & 1-\mu_m & 0 & 0 & 0 \\ 0 & 0 & 0 & \frac{1-2\mu_m}{2} & 0 & 0 \\ 0 & 0 & 0 & 0 & \frac{1-2\mu_m}{2} & 0 \\ 0 & 0 & 0 & 0 & 0 & \frac{1-2\mu_m}{2} \end{bmatrix} \tag{15}$$

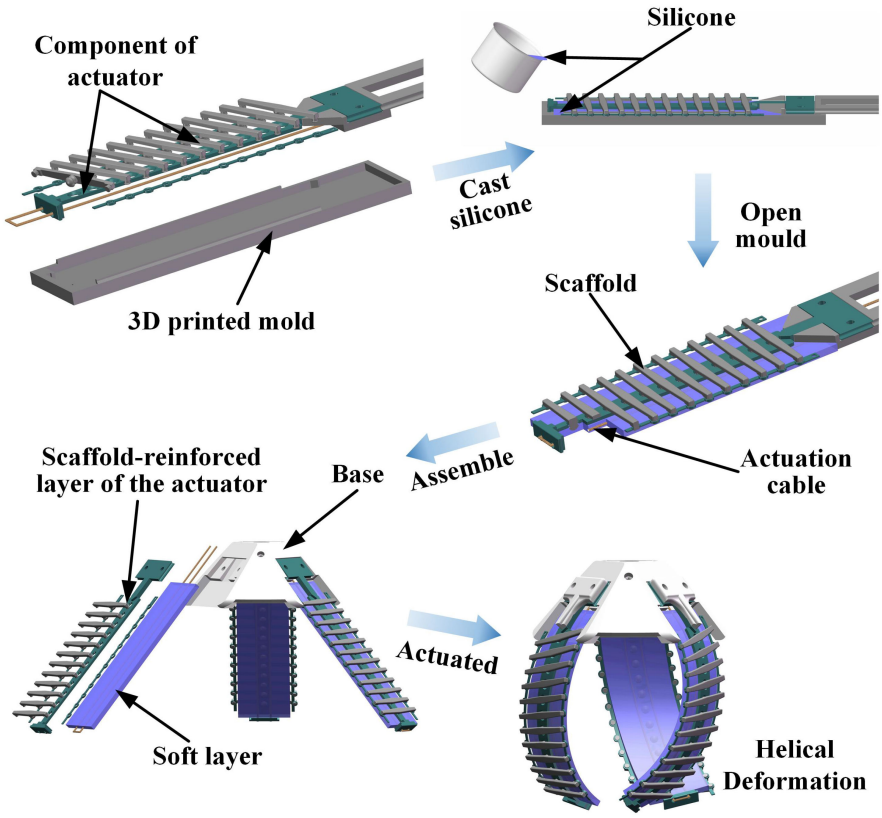

Fig. 5. Scaffold reinforcement soft actuator fabrication process.

material. Therefore, the corresponding stiffness matrix can be formulated as

For the second layer, $i = 2$, the corresponding stiffness matrix is $\boldsymbol{C}^{(2)}$. Since the scaffold reinforcement layer consists of anisotropic material, the corresponding stiffness matrix cannot be obtained directly as (15) shown at the bottom of the previous page. According to [47], $\boldsymbol{\sigma} = \boldsymbol{C}\boldsymbol{\varepsilon}$ and $\boldsymbol{\varepsilon} = \boldsymbol{S}\boldsymbol{\sigma}$; the relation between stiffness coefficient matrix $\boldsymbol{C}$ and the compliance coefficient matrix $\boldsymbol{S}$ can be formulated as

$$\boldsymbol{C^{(2)}} = \boldsymbol{S}^{-1} = \begin{bmatrix} S_{11} & S_{12} & S_{13} & 0 & 0 & 0 \\ S_{12} & S_{22} & S_{23} & 0 & 0 & 0 \\ S_{13} & S_{23} & S_{33} & 0 & 0 & 0 \\ 0 & 0 & 0 & S_{44} & 0 & 0 \\ 0 & 0 & 0 & 0 & S_{55} & 0 \\ 0 & 0 & 0 & 0 & 0 & S_{66} \end{bmatrix}^{-1}. \quad (16)$$

The computation of $\boldsymbol{C}^{(2)}$ can be converted as the computation of the corresponding $\boldsymbol{S}$. Generally, the compliance coefficient S_{ij} can be obtained by the engineering constant. According to the consequences of linearity [51], the same direction strain produced by independent stress can be superposed. Consequently, when three sets of loads are applied on the element of a cube in the scaffold reinforcement layer, the strain ε_{11} in the direction of the x-axis can be superposed by three sets of strain, which are denoted as ε_{11}^x, ε_{11}^y, and ε_{11}^z, respectively. Note that ε_{11}^x is equal to σ_{11}/E_1, where σ_{11} represents the stress along the x-axis, and E_1 represents Young's modulus in the x-axis. ε_{11}^y is equal to $-\sigma_{22}\mu_{21}/E_2$, where E_2 denotes Young's modulus in the y-axis and μ_{21} is the Poisson ratio, which is the ratio of the transverse strain ε_{11} to the principal strain ε_{22} during the plane state of stress, and can be obtained as

$$\mu_{21} = -\frac{\varepsilon_{11}}{\varepsilon_{22}}. \quad (17)$$

ε_{11}^z can be obtained in the same way as ε_{11}^y. Consequently, the strain can be formulated as

$$\varepsilon_{11} = \varepsilon_{11}^x + \varepsilon_{11}^y + \varepsilon_{11}^z = \frac{\sigma_{11}}{E_1} - \frac{\sigma_{22}\mu_{21}}{E_2} - \frac{\sigma_{33}\mu_{31}}{E_3}. \quad (18)$$

Similarly, the strains ε_{22} and ε_{33} can be formulated as

$$\varepsilon_{22} = -\frac{\sigma_{11}\mu_{12}}{E_1} + \frac{\sigma_{22}}{E_2} - \frac{\sigma_{33}\mu_{32}}{E_3} \quad (19)$$

$$\varepsilon_{33} = -\frac{\sigma_{11}\mu_{13}}{E_1} - \frac{\sigma_{22}\mu_{23}}{E_2} + \frac{\sigma_{33}}{E_3}. \quad (20)$$

The shearing strain can be obtained based on the engineering constant of orthotropic material and set of loads

$$2\varepsilon_{12} = \frac{\sigma_{12}}{G_{12}},\ 2\varepsilon_{13} = \frac{\sigma_{13}}{G_{13}},\ 2\varepsilon_{23} = \frac{\sigma_{23}}{G_{23}} \quad (21)$$

where $2\varepsilon_{ij}$ represents the variation of angle between two directions, the shear stress is denoted as σ_{ij}, and the shearing modulus is denoted as G_{ij}; i and j represent corresponding directions.

Based on (17)–(21), $\boldsymbol{S}$ can be obtained as

$$\boldsymbol{S}=\begin{bmatrix} \frac{1}{E_1} & -\frac{\mu_{21}}{E_2} & -\frac{\mu_{31}}{E_3} & 0 & 0 & 0 \\ -\frac{\mu_{12}}{E_1} & \frac{1}{E_2} & -\frac{\mu_{32}}{E_3} & 0 & 0 & 0 \\ -\frac{\mu_{13}}{E_1} & -\frac{\mu_{23}}{E_2} & \frac{1}{E_3} & 0 & 0 & 0 \\ 0 & 0 & 0 & \frac{1}{G_{23}} & 0 & 0 \\ 0 & 0 & 0 & 0 & \frac{1}{G_{13}} & 0 \\ 0 & 0 & 0 & 0 & 0 & \frac{1}{G_{12}} \end{bmatrix}. \quad (22)$$

The nine independent material coefficients of the scaffold reinforcement layer $\boldsymbol{S}$ can be obtained based on the rule of the mixture and uniaxial tension tests. The description of test methods and the calculations of the nine independent coefficients of the scaffold reinforcement layer are detailed in the Appendix. According to the principle of superposition [47], the corresponding stiffness coefficient matrix $\boldsymbol{C^{(2)}}$ can be obtained to calculate the elastic potential energy of the second layer.

The soft layer and the scaffold reinforcement layer are isotropic elastic; the fourth-order stiffness coefficient matrix $\boldsymbol{C^{(1)}}$ can be obtained based on Young's modulus E_m and the Poisson ratio μ_m. In addition, Young's modulus and the Poisson ratio of silicone rubber (Ecoflex 00-30) are $E_m = 68$ kPa and $\mu_m = 0.48$, respectively, which are provided in the Ecoflex Series technical overview [52]. According to the minimum potential energy method, the elastic potential energy U_1 stored in the first layer can be expressed in tensor form as

$$U_1=\int_{-h_1}^{0}\frac{1}{2}\varepsilon^{(1)}:C^{(}1):\varepsilon^{(1)}dv_1=\frac{LW}{2}\int_{-h_1}^{0}\varepsilon_{ij}\sigma_{ij}dz. \quad (23)$$

The elastic potential energy U_2 stored in the second layer can be expressed as (tensor form)

$$U_2=\int_{-H}^{-h_1}\frac{1}{2}\varepsilon^{(2)}:C^{(2)}:\varepsilon^{(2)}dv_2=\frac{LW}{2}\int_{-H}^{-h_1}\varepsilon_{ij}\sigma_{ij}dz \quad (24)$$

where the expression of the elastic potential energy of the dual-layer actuator is tensor form, which can be transformed into scalar form according to the tensor analysis [49].

Based on the elastic mechanics' analysis of the soft layer, the normal strain magnitude is $\varepsilon_{11}=\varepsilon_{11}^{r}\cos^2\varphi+\varepsilon_{22}^{r}\sin^2\varphi$. Since the offset value between the upper surface and the actuation cable is h_u according to actuator design, the actuation cable displacement driven by the external motor is $\Delta L_a = L\cdot\varepsilon_{11}|_{z=-h_u}$. According to (10), the energy consumption of motor W_c can be formulated as

$$W_c=LF_c\left[(e_{11}-h_u\kappa_1)\cos^2\varphi+(e_{22}-h_u\kappa_2)\sin^2\varphi\right]. \quad (25)$$

Based on the mechanics' analysis, the potential energy (8) includes seven unknown variables, and the potential energy can be formulated as a variable function, denoted as $\prod(e_{11},\ e_{22},\ e_{33},\ \kappa_1,\ \kappa_2,\ q,\ \varphi)$. According to the elasticity theory [53], the potential energy should have a local minimum value when the boundary conditions of the elastic actuator are satisfied. Therefore, the energy optimization in every dimension should be achieved, and the optimal solution is

$$\frac{\partial\prod}{\partial e_{11}}=0\ ,\ \frac{\partial\prod}{\partial e_{22}}=0\ ,\ \frac{\partial\prod}{\partial e_{33}}=0\ ,\ \frac{\partial\prod}{\partial\kappa_1}=0$$
$$\frac{\partial\prod}{\partial\kappa_2}=0\ ,\ \frac{\partial\prod}{\partial q}=0\ ,\ \frac{\partial\prod}{\partial\varphi}=0\ . \quad (26)$$

By resolving (26), the value of variables $e_{11},\ e_{22},\ e_{33},\ \kappa_1,\ \kappa_2,\ q$, and φ can be numerically solved. It is worth noting that $\kappa_1,\ \kappa_2$, and φ can determine the posture of the actuator. Based on the geometrical characteristics of the helical curve [48], the value of pitch P can be formulated as

$$P=\pi\left|\frac{(\kappa_1-\kappa_2)\sin 2\varphi}{\kappa_1^2\cos^2\varphi+\kappa_2^2\sin^2\varphi}\right| \quad (27)$$

where P is positive if the actuator twists toward a positive Y-direction. Meanwhile, the radius can be obtained as follows:

$$R=\frac{\kappa_1\cos^2\varphi+\kappa_2\sin^2\varphi}{\kappa_1^2\cos^2\varphi+\kappa_2^2\sin^2\varphi}. \quad (28)$$

Based on the mechanical model, the helical posture of the actuator can be determined by the tension of the actuation cable and the scaffold deflection. Correspondingly, the deformation behavior of the actuator can be predicted, which provides the foundation for actuator control.

IV. Fabrication

A prototype of the proposed soft actuator was fabricated to verify the validity of the proposed model. Meanwhile, a soft gripper based on the scaffold-reinforced actuator was manufactured simultaneously. The scaffold-reinforced actuators and the soft gripper base were fabricated separately. The multistep approach of assembly and molding was adopted to fabricate the actuator, as shown in Fig. 5. The components of the soft actuator and the base were fabricated by A8 FDM commercial 3-D printer, which is produced by Shenzhen Aurora Technology Co., Ltd. (Shenzhen, China). The spine and flexible linkage were made by thermoplastic polyurethane elastomer (TPU), while the scaffold, soft gripper base, and mold were made by polylactic acid material (PLA). The fabrication technique of the proposed gripper is comprised of four parts: First, the nylon thread was coated with petroleum jelly in advance, which could avoid friction between the silicone and the nylon thread. Second, the nylon was threaded through the reserved hole. Then, the scaffolds, spine, flexible linkage, and mold were assembled based on the designed structure to define the contour of the structure of the actuator and the silicone rubber (Ecoflex-0030 silicone, A/B, Smooth-on, Inc., Macungie, PA, USA) cured inside the assembled mold. It should be mentioned that the soft layer is adhered to the scaffold-reinforced layer by the Sil-Poxy (Smooth-on, Inc., Macungie, PA, USA). Finally, three actuators were fixed on the base of the soft gripper to complete the assembly, as shown in Fig. 5.

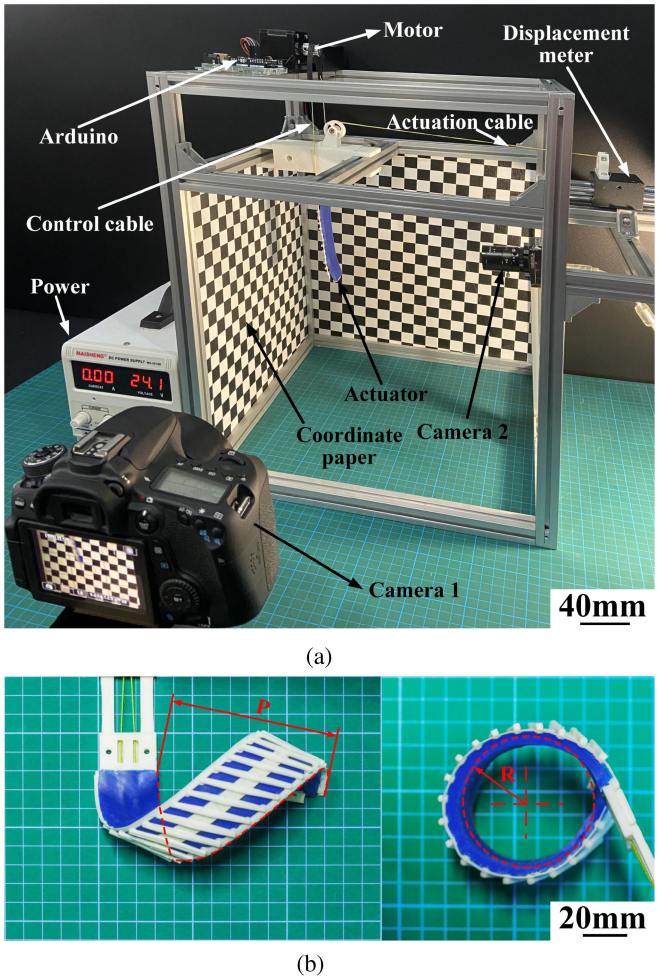

Fig. 6. Experiment environment. (a) Experiment platform. (b) Measurements of radius and pitch based on the visual feedback.

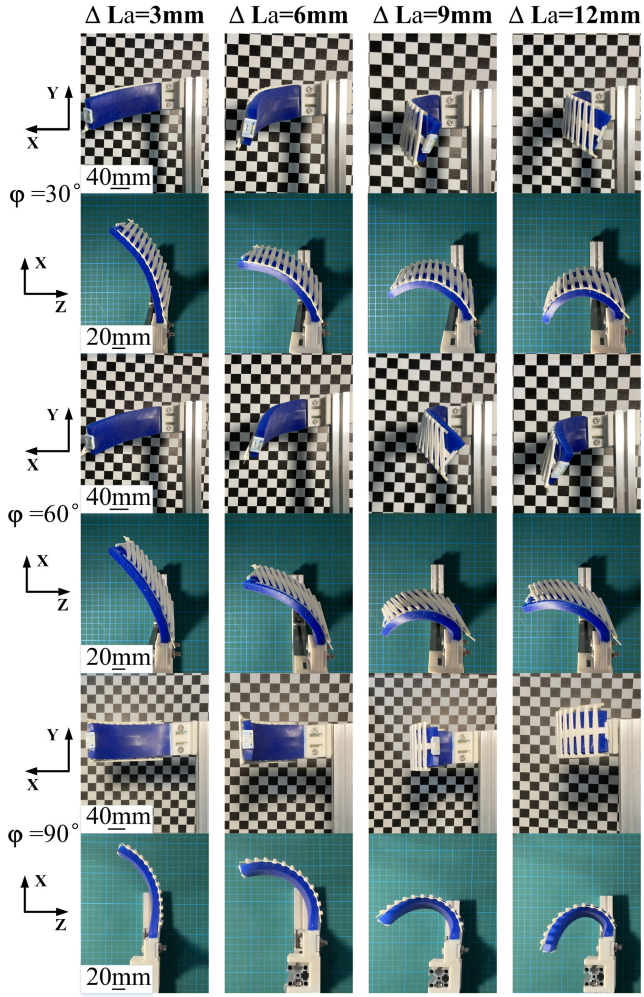

Fig. 7. Performance of the actuator under different deflection angles φ (30°, 60°, and 90°) and different cable displacements ΔL_a (3 mm, 6 mm, 9 mm, and 12 mm).

V. Experiments

Experiments were conducted to verify the proposed model of the scaffold reinforcement actuator and the grasping performance of the gripper.

A. Experiment Environment

An experiment platform was developed, as shown in Fig. 6. The proximal end of the proposed actuator was clamped in a rigid fixture, and the distal end can bend or twist freely. The two ends of the actuation cables were fixed to the shaft of a stepper motor (controlled by Arduino control board). The control cables were connected in the same way. The coordinate paper was set in the front and left to the actuator to record the actuator's position during deformation. Two high-definition cameras (DSLR, Rebel T5i, Canon Inc., New York, NY, USA) were adopted to monitor the actuator from the front and the side. Radius and pitch values of the actuator can be obtained based on the pictures from the two cameras, as shown in Fig. 6.

Fig. 7 shows the performance of the actuator under different angles φ and different cable displacements ΔL_a. In general, the actuator conducted pure bending when the direction of the scaffolds was perpendicular to the spine. Otherwise, the actuator curled a helix. It is worth mentioning that the scaffolds are always parallel to the axis of the helix no matter what the value of the deflection angle is. More discussed details will appear in Section V-B1 that follow.

B. Model Verification

1) Kinematic Model: The deflection angle φ was set as 30°, 45°, 60°, 75°, and 90°, respectively, and the actuator was driven by the reduction length ranging from 1 to 10 mm at an interval of 1 mm. Fig. 8(a)–(e) shows that the helical radius is inversely proportional to the cable displacement ΔL_a. The deflection angle φ does not contribute to the value of the radius, which is consistent with the theoretical result.

It is worth noting that the experimental radius value is always larger than the theoretical one, and the maximum deviation can reach 30%. This phenomenon can be explained as that (5) is obtained because h_c does not change during the deformation. However, the soft layer is compressed during the deformation; as a result, h_c increases. Thus, the actual value of the radius

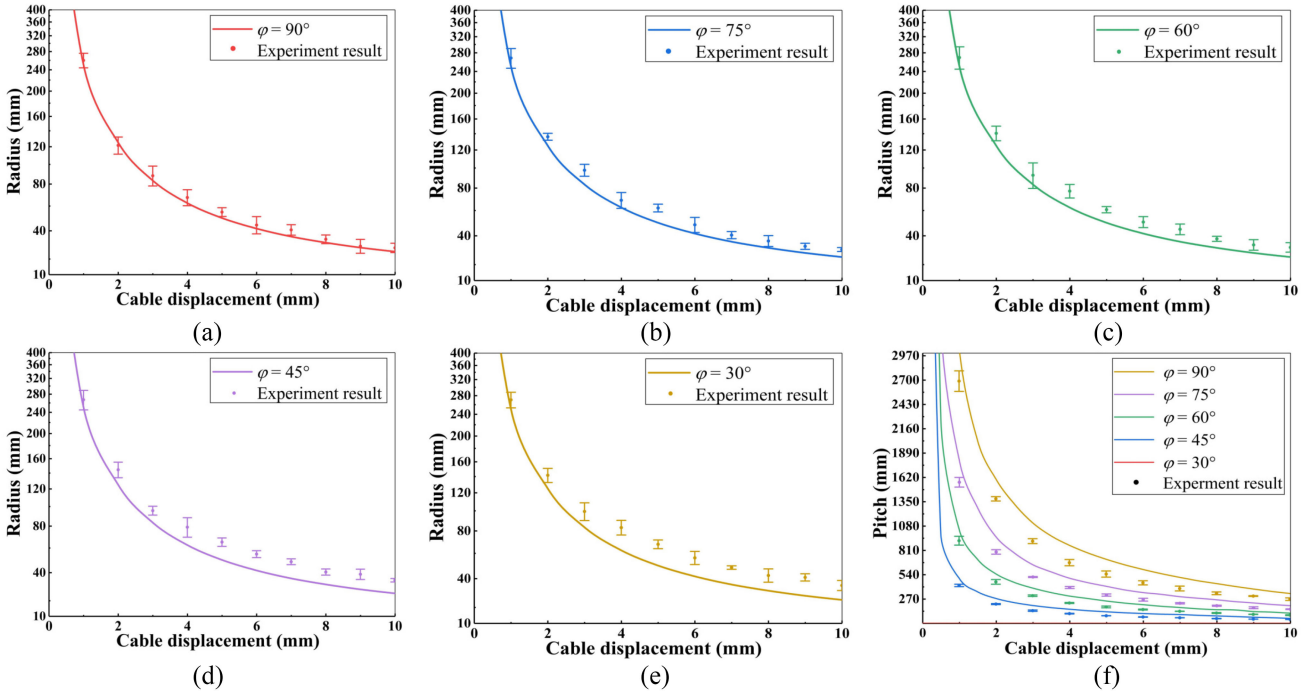

Fig. 8. Experimental result of kinematic model verification. (a)–(e) Theory curves and experimental results of the radius with $\varphi = 30°$, $\varphi = 45°$, $\varphi = 60°$, $\varphi = 75°$, and $\varphi = 90°$. (f) Variation of the pitch with the actuation cable displacement.

is larger than the value obtained based on (5). Another reason for the discrepancies between the theoretical value and the actual one is that the bending deformation in the y-direction is ignored, namely, κ_2 is regarded as zero in the kinematic model. Correspondingly, the theoretical value equals $1/\kappa_1$, which is smaller than the value obtained (28).

The pitch curve of the helical motion is plotted in Fig. 8(f). It reveals that the helical pitch has a negative correlation with the cable displacement ΔL_a on the condition that the deflection angle φ keeps constant. Meanwhile, the helical pitch decreases as the deflection angle increases. There also exist differences between the actual values and the theoretical ones. The same as before, the differences can be explained as the offset between the actuation cable and the spine increases during the deformation process, which makes the actual pitch value larger than the theoretical one. It should be cautioned that the difference between the actual value of the pitch and the theoretical one is larger when the deflection angle is smaller. This is because $\varphi + \theta = \pi/2$ is applied to obtain (7). However, the actual value of $\varphi + \theta$ might not equal $\pi/2$.

To investigate the actual value of $\varphi + \theta$, a repeatability test was carried out, in which the actuator repeated to twist under 6-mm cable displacement for 25 times. The corresponding test results are shown in Table I, which demonstrates that $\varphi + \theta$ is always less $\pi/2$, and the gap increases as the deflection angle decreases. This phenomenon can be explained as that $\varphi + \theta = \pi/2$ is obtained based on the unfolded drawing of the actuator. It holds based on the two assumptions: 1) the deflection angle remains constant during the deformation process; and 2) the actuator along the y-direction does not deform, namely, $\kappa_2 = 0$. There still exist angular rotations of scaffolds despite the existence of friction between the scaffolds and the soft layer. Furthermore, there exists deformation along the y-direction during the helical deformation process. The effect of deformation along the y-direction becomes more significant as the twist deformation increases. This explains why the gap between $\varphi + \theta$ and $\pi/2$ increases as the deflection angle decreases.

TABLE I
REPEATABILITY TEST

Deflection angle	The sum of deflection and helical angle					SD
	First	Second	Third	Fourth	Fifth	
30°	76.9°	76.4°	75.6°	75.4°	76.7°	0.53
45°	80.3°	81.6°	80.7°	80.3°	81.1°	0.50
60°	84.2°	83.5°	85°	84.3°	84.6°	0.50
75°	87.4°	87.6°	87.1°	87.5°	86.9°	0.26
90°	90°	90°	90°	90°	90°	0

2) Mechanical Model: To verify the validity of the proposed mechanical model, experiments with five groups of different deflection angles were conducted. A force-meter (HANDPI, SH-100, range: 100 N, accuracy: 0.01% F.S.) was connected to the actuation cable to measure the internal tension of the actuation cable. The experimental results of the actual helical radius are shown in Fig. 9, which demonstrates that the helical radius is inversely proportional to the tension. Meanwhile, the radius decreases as the deflection angle increases when the tension is the same. This can be explained as that curvature κ_1 increases as the deflection angle increases, and $\kappa_1 \gg \kappa_2$; the radius is mainly determined by curvature κ_1. Namely, the radius has a negative correlation with κ_1 according to (28). Therefore, the radius decreases as the deflection angle increases.

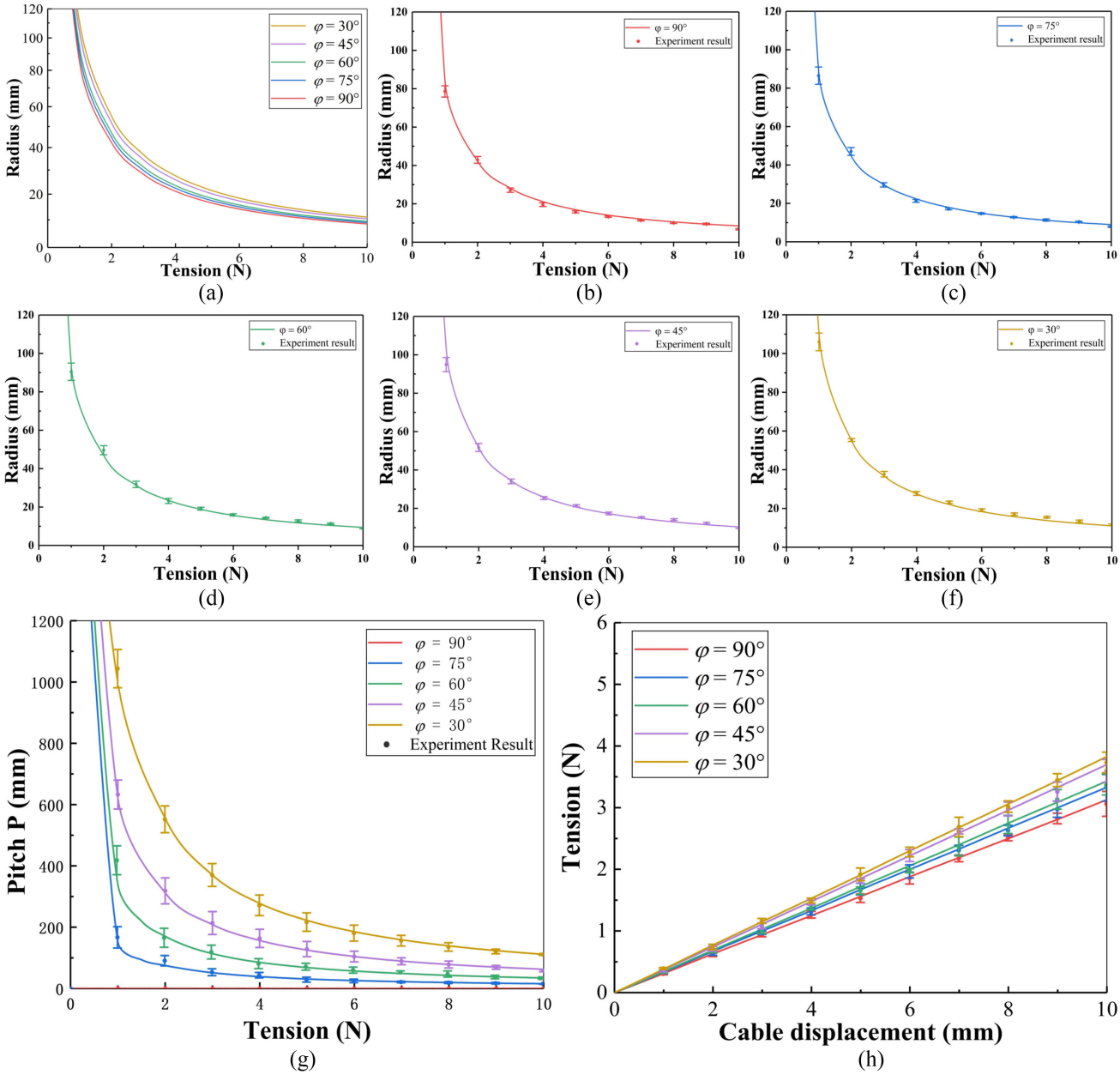

Fig. 9. Theoretical and experimental results of the helical deformation actuator shown in (a)–(g) with $\varphi = 30°$, $\varphi = 45°$, $\varphi = 60°$, $\varphi = 75°$, and $\varphi = 90°$. (a) Theoretical deformation curves of radius, which are different deflection angles, change as the different tension based on the mechanical model. The error bar and the theoretical value are depicted in (b)–(f). The solid line shows the theoretical value, and the point shows the experiment result in the same deflection. The experiment result and the theoretical value are shown in (g), same as before. (h) shows the elastic relationship between cable displacement and tension of the actuator. It shows the theoretical and experimental results of the elastic of the actuator with different deflection angles.

The experimental values are close to the theoretical one, and the deviation value is much smaller than the one based on the kinematic model. However, the deviation value is relatively larger on the condition that tension is small. The maximum value of the root-mean-square error in the mechanical is 4.57. The reason is that the measurement error is more significant once the deformation of the actuator is small.

Fig. 9(g) demonstrates that the helical pitch has a negative correlation with the tension on the condition that the deflection angle φ remains constant, and the helical pitch does not change significantly when the tension force is over 8 N. Meanwhile, the helical pitch increases as the deflection angle φ decreases. It is worth noting that significant deviations still exist between the actual values and the theoretical ones when the tension force is slight. This can be explained as that the helical pitch cannot be measured accurately when the deformation of the actuator is less than a circle of spiral.

Compared with Figs. 8(f) and 9(g), it can be found that the pitch trends are similar as the actuator was actuated by the cable displacement and the tension, respectively. Fig. 9(h) reveals that the cable displacement changes linearly as the tension changes for the given pitch. This can be explained as follows: as the

Fig. 10. Grasping performance of the gripper in the different attitude. (a) Grasping a wood square piece, ping-pong ball, injector (26.5 g), and glue straw in the attitude that the scaffolds of fingers 1, 2, and 3 are perpendicular to the spine. (b) Grasping a video disc, packaging tape (253.2 g), plastic box, and stepper motor driver in the attitude that the scaffolds of fingers 1 and 2 are not perpendicular to the spine, while finger 3 is perpendicular to the spine. (c) Grasping a stepper motor (374.1 g), lemon, screwdriver, and stapler in the attitude that the scaffolds of fingers 1, 2, and 3 are not perpendicular to the spine. (d) Unscrewing a bottle cap.

material parameters and the deflection angle of the scaffolds are determined, curvatures κ_1 and κ_2 can be formulated as proportion functions of the tension according to the solution of (26). According to (27), therefore, P can be formulated as $P = c/F$, and the proportional coefficient c can be obtained based on the material parameters and the deflection angle. Meanwhile, $P \propto 1/\Delta L_a$ according to the geometric constraint (7). Correspondingly, $F \propto \Delta L_a$.

These results demonstrate that the proposed actuator is endowed with linear elastic property to some extent, and the elasticity coefficient is determined once the design parameters and the deflection angle are determined. The linear elastic property provides a convenient way to realize the mechanical control of the proposed actuator. First, the kinematic method can be adopted to calculate ΔL_a; then, the actuation tension can be obtained based on the corresponding elasticity coefficient of the actuator. This method can avoid the intensive calculation of solving (26). However, the ignorance of bending deformation in the y-direction results in the deviation between the actual cable displacement and the theoretical one to achieve the desired deformation, which might limit the control precision.

C. Grasping Experiments

To verify the dexterity of the proposed actuator, objects of various natures were grasped by the prototype gripper fabricated in Section IV. We define the actuator on the front left and the front right of the base as fingers 1 and 2, respectively. In contrast, the other actuator on the behind of the base is finger 3; the corresponding deflection angles of the three fingers are defined as φ_1, φ_2, and φ_3, respectively. The grasping performance, as shown in Fig. 10, demonstrated that the proposed actuator can adjust the attitude via switching of the scaffolding mechanism in real-time situations according to the shape of the objects (see supplementary video, S1). Fig. 10(a) presents the grasping of a wood square piece, a ping-pong ball, an injector, and a glue straw, respectively ($\varphi_1 = \varphi_2 = \varphi_3 = 90^\circ$). Three actuators conducted pure bending to grasp these

regular shape objects. Fig. 10(b) demonstrates the grasping of a video disc, a packaging tape, a plastic box, and a stepper motor driver ($\varphi_1 = \varphi_2 = 50^\circ$ and $\varphi_3 = 90^\circ$). These objects are characterized by flat shape. Owing to the scaffold-reinforced mechanism, two actuators could achieve helical motion, while the other actuator conducted pure bending motion. As a result, three actuator tips were arranged almost in line. This behavior can increase the contact area to improve grasping stability for the flat-shaped or cylindrical-shaped objects. Fig. 10(c) shows the grasping of a stepper motor, a lemon, a screwdriver, and a stapler ($\varphi_1 = \varphi_2 = \varphi_3 = 45^\circ$). These irregular, slender shapes, and heavier objects are grasped based on the helical motions of the three actuators, since the helical motion can increase the contact surface of the actuator, which will directly increase the friction between the object and the actuator. Fig. 10(d) displays the process of unscrewing the bottle cap ($\varphi_1 = \varphi_2 = 30^\circ$). Since the actuators with helical deformation can provide the normal bending actuation force and a friction force in the transverse direction, the corresponding resultant force can be adjusted along the thread rotation direction of the bottle cap. Hence, the bottle cap can be completely unscrewed by the actuators. The grasping test and the unscrewing test are shown in the supplementary material (see supplementary video, S1).

VI. Conclusion

To achieve high compliance, adaptability, and easy controllability, the soft actuator usually preprograms the desired motions into the flexible structures, which can realize specific motion at a low cost. However, the preprogrammed structure also constrains the motion diversity of the actuator. Therefore, this article proposed a scaffold reinforcement actuator, rotatable scaffolds were uniformly distributed on the surface of the soft layer, and the different deflection angles of the scaffolds can provide deformation constraints in different directions. The actuator can achieve various helical motions in the 3-D space, and the bending and helical motions can be decoupled by adequately adjusting the orientation of the scaffolds.

Based on the geometrical feature of the scaffold-reinforced actuator, the kinematic model was developed to predict the behavior with explicit relationships between the actuation cable displacement, deflection angle, helical radius, and pitch. Furthermore, a mechanical model was also proposed to quantify the relationships between drive force, deflection angle, helical radius, and pitch, which can forecast the performance of the actuator under a given driven force and deflection angle. In addition, actuators were fabricated to verify the validity of the proposed models. The experimental results demonstrate that both the kinematic and mechanical models can predict the helical motion of the actuator with reasonable accuracy. Finally, the fabricated gripper can grasp a variety of irregularly shaped objects by means of adjusting the attitude of its fingers. Hence, its enhanced universality can be adopted in applications where both high versatility and flexibility are required.

Although the gripper can grasp various irregularly shaped objects, there are still some drawbacks to our current gripper. For example, the load capacity of the gripper is limited because the scaffold reinforcement layer is composed of many joints and links, which are not robust against an external force. In future work, we will increase the load capacity of the gripper by exploring the influence of different materials of two layers and optimizing the structure of the scaffold reinforcement layer.

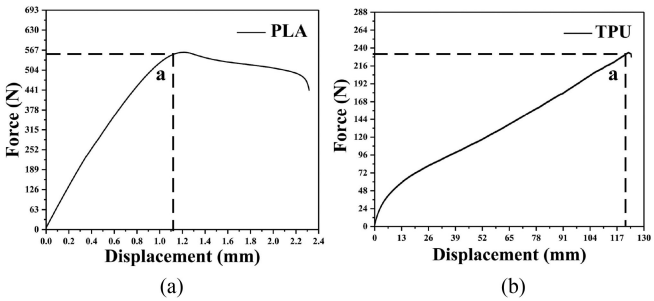

(a) (b)

Fig. 11. Experimental results of uniaxial tensile test for (a) PLA and (b) TPU.

Appendix

The stress–strain relationship of the PLA and TPU was experimentally obtained by uniaxial tension tests that were conducted using an electromechanical universal testing machine (CMT5540, MTS Systems (China) Co., Ltd., Shanghai, China) according to the ISO 37 standard, where the samples were stretched at a rate of 1 mm/min at room temperature. Moreover, the uniaxial tension tests of PLA and TPU were repeated four times (see supplementary material S2), and the average experimental stress–strain data are shown in Fig. 11. Based on the mechanics of materials [54], the stress is directly proportional to the strain in the elastic stage, and if the axial loading of the material exceeds the proportional limit, the yield of the materials shows serious plastic deformation, which will affect the normal work of the materials. Hence, Young's modulus of PLA and TPU in the elastic stage was measured as $E_p \approx 1.4$ GPa and $E_t \approx 6.0$ MPa, respectively. The Poisson ratios of PLA and TPU used in the model are $\mu_p = 0.48$ and $\mu_t = 0.46$, respectively. Assume the volume fraction of the PLA and TPU in the scaffold reinforcement layer is 50%, respectively. The shear modulus for PLA and TPU can be calculated by $G_p = E_p/(2 + 2\mu_p)$ and $G_t = E_t/(2 + 2\mu_t)$, respectively. The nine independent material coefficients of the scaffold reinforcement layer are calculated according to the rule of the mixture as

$$E_1 = E_p V_p + E_t V_t, E_2 = \frac{E_p E_t}{E_p V_t + E_t V_p}, E_3 = E_2 \quad \text{(A1)}$$

$$G_{12} = G_p V_p + G_t V_t, G_{13} = G_{12}, G_{23} = G_t \quad \text{(A2)}$$

$$\mu_{12} = \mu_p V_p + \mu_t V_t, \mu_{13} = \mu_{12}, \mu_{23} = \mu_t. \quad \text{(A3)}$$

References

[1] I. Gaiser et al., "A new anthropomorphic robotic hand," in *Proc. 8th IEEE-RAS Int. Conf. Humanoid Robots*, 2008, pp. 418–422.

[2] H.-S. Kim, J.-Y. Lee, W.-S. Chu, and S.-H. Ahn, "Design and fabrication of soft morphing ray propulsor: Undulator and oscillator," *Soft Robot.*, vol. 4, no. 1, pp. 49–60, 2017.

[3] Y. Yang, Y. Chen, Y. Li, M. Z. Q. Chen, and Y. Wei, "Bioinspired robotic fingers based on pneumatic actuator and 3D printing of smart material," *Soft Robot.*, vol. 4, no. 2, pp. 147–162, 2017.

[4] Y. Li, Y. Chen, T. Ren, Y. Li, and S. H. Choi, "Precharged pneumatic soft actuators and their applications to untethered soft robots," *Soft Robot.*, vol. 5, no. 5, pp. 567–575, 2018.

[5] Y. Li, Y. Chen, and Y. Li, "Pre-charged pneumatic soft gripper with closed-loop control," *IEEE Robot. Autom. Lett.*, vol. 4, no. 2, pp. 1402–1408, Apr. 2019.

[6] R. Chen, L. Wu, Y. Sun, J.-Q. Chen, and J.-L. Guo, "Variable stiffness soft pneumatic grippers augmented with active vacuum adhesion," *Smart Mater. Struct.*, vol. 29, no. 10, 2020, Art. no. 105028.

[7] X. Wang, A. Khara, and C. Chen, "A soft pneumatic bistable reinforced actuator bioinspired by venus flytrap with enhanced grasping capability," *Bioinspiration Biomimetics*, vol. 15, no. 5, 2020, Art. no. 056017.

[8] Y. Chen, H. Chung, B. Chen, and B. Baoyinjiya, "A lobster-inspired articulated shaft for minimally invasive surgery," *Robot. Auton. Syst.*, vol. 131, 2020, Art. no. 103599.

[9] Y. Chen, H. Chung, B. Chen, B. Baoyinjiya, and Y. Sun, "A lobster-inspired bending module for compliant robotic applications," *Bioinspiration Biomimetics*, vol. 15, no. 5, 2020, Art. no. 056009.

[10] X. Ni et al., "Experimental study of multi-stable morphing structures actuated by pneumatic actuation," *Int. J. Adv. Manuf. Technol.*, vol. 108, no. 4, pp. 1203–1216, 2020.

[11] H. Li, J. Yao, P. Zhou, W. Zhao, Y. Xu, and Y. Zhao, "Design and modeling of a high-load soft robotic gripper inspired by biological winding," *Bioinspiration Biomimetics*, vol. 15, no. 2, 2020, Art. no. 026006.

[12] H. In, B. B. Kang, M. Sin, and K.-J. Cho, "Exo-Glove: A wearable robot for the hand with a soft tendon routing system," *IEEE Robot. Autom. Mag.*, vol. 22, no. 1, pp. 97–105, Mar. 2015.

[13] J. Li, G. Zhong, H. Yin, M. He, Y. Tan, and Z. Li, "Position control of a robot finger with variable stiffness actuated by shape memory alloy," in *Proc. IEEE Int. Conf. Robot. Autom.*, 2017, pp. 4941–4946.

[14] V. Vikas, E. Cohen, R. Grassi, C. Sozer, and B. Trimmer, "Design and locomotion control of a soft robot using friction manipulation and motor-tendon actuation," *IEEE Trans. Robot.*, vol. 32, no. 4, pp. 949–959, Aug. 2016.

[15] L. Li, W. Ma, Q. Zhang, G. Yuan, H. Li, and Y. Tian, "Research on the mechanism of variable stiffness of the twisted and coiled polymer actuator during saturated contraction," *Smart Mater. Struct.*, vol. 29, no. 6, 2020, Art. no. 065014.

[16] T. S. Zhang, A. Kim, M. Ochoa, and B. Ziaie, "Controllable 'somersault' magnetic soft robotics," in *Proc. 28th IEEE Int. Conf. Micro Electro Mech. Syst.*, 2015, pp. 1044–1047.

[17] T. Li, C. Keplinger, R. Baumgartner, S. Bauer, W. Yang, and Z. Suo, "Giant voltage-induced deformation in dielectric elastomers near the verge of snap-through instability," *J. Mech. Phys. Solids*, vol. 61, no. 2, pp. 611–628, 2013.

[18] R. Chen et al., "Bio-inspired shape-adaptive soft robotic grippers augmented with electroadhesion functionality," *Soft Robot.*, vol. 6, pp. 701–712, 2019.

[19] R. Chen et al., "Magnetically controllable liquid metal marbles," *Adv. Mater. Interfaces*, vol. 6, 2019, Art. no. 1901057.

[20] J. Wissman, A. Ikei, S. G. Konarski, C. A. Rohde, and C. J. Naify, "Tunable acoustics with dielectric elastomer activated granular jamming exhibiting a solid-fluid transition," *J. Appl. Phys.*, vol. 128, no. 20, 2020, Art. no. 204901.

[21] M. Wehner et al., "An integrated design and fabrication strategy for entirely soft, autonomous robots," *Nature*, vol. 536, no. 7617, pp. 451–455, 2016.

[22] B. Mosadegh et al., "Pneumatic networks for soft robotics that actuate rapidly," *Adv. Function. Mater.*, vol. 24, no. 15, pp. 2163–2170, 2014.

[23] W. Felt, "Folded-tube soft pneumatic actuators for bending," *Soft Robot.*, vol. 6, no. 2, pp. 174–183, 2019.

[24] J. Bishop-Moser, G. Krishnan, C. Kim, and S. Kota, "Design of soft robotic actuators using fluid-filled fiber-reinforced elastomeric enclosures in parallel combinations," in *Proc. IEEE/RSJ Int. Conf. Intell. Robots Syst.*, 2012, pp. 4264–4269.

[25] K. C. Galloway, P. Polygerinos, C. J. Walsh, and R. J. Wood, "Mechanically programmable bend radius for fiber-reinforced soft actuators," in *Proc. 16th Int. Conf. Adv. Robot.*, 2013, pp. 1–6.

[26] Y. Li, Y. Chen, Y. Yang, and Y. Wei, "Passive particle jamming and its stiffening of soft robotic grippers," *IEEE Trans. Robot.*, vol. 33, no. 2, pp. 446–455, Apr. 2017.

[27] P. Jiang, Y. Yang, M. Z. Q. Chen, and Y. Chen, "A variable stiffness gripper based on differential drive particle jamming," *Bioinspiration Biomimetics*, vol. 14, no. 3, 2019, Art. no. 036009.

[28] Y. Zhao et al., "A soft continuum robot, with a large variable stiffness range, based on jamming," *Bioinspiration Biomimetics*, vol. 14, no. 6, 2019, Art. no. 066007.

[29] S. G. Fitzgerald, G. W. Delaney, and D. Howard, "A review of jamming actuation in soft robotics," *Actuators*, vol. 9, 2020, Art. no. 104.

[30] S.-Q. An, H.-L. Zou, Z.-C. Deng, and D.-Y. Guo, "Damping effect of particle-jamming structure for soft actuators with 3D-printed particles," *Smart Mater. Struct.*, vol. 29, no. 9, 2020, Art. no. 095012.

[31] Y. Yang, Z. Kan, Y. Zhang, Y. A. Tse, and M. Y. Wang, "A novel variable stiffness actuator based on pneumatic actuation and supercoiled polymer artificial muscles," in *Proc. Int. Conf. Robot. Autom.*, 2019, pp. 3983–3989.

[32] P. Bilancia and G. Berselli, "Design and testing of a monolithic compliant constant force mechanism," *Smart Mater. Struct.*, vol. 29, no. 4, 2020, Art. no. 044001.

[33] Q. Guan, J. Sun, Y. Liu, N. M. Wereley, and J. Leng, "Novel bending and helical extensile/contractile pneumatic artificial muscles inspired by elephant trunk," *Soft Robot.*, vol. 7, no. 5, pp. 597–614, 2020.

[34] J. Chandler, M. Chauhan, N. Garbin, K. L. Obstein, and P. Valdastri, "Parallel helix actuators for soft robotic applications," *Front. Robot. AI*, vol. 7, 2020, Art. no. 119.

[35] L. Ge, T. Wang, N. Zhang, and G. Gu, "Fabrication of soft pneumatic network actuators with oblique chambers," *J. Vis. Exp.*, vol. 138, 2018, Art. no. e58277.

[36] J. Realmuto and T. Sanger, "A robotic forearm orthosis using soft fabric-based helical actuators," in *Proc. 2nd IEEE Int. Conf. Soft Robot.*, 2019, pp. 591–596.

[37] T. Wang, L. Ge, and G. Gu, "Programmable design of soft pneu-net actuators with oblique chambers can generate coupled bending and twisting motions," *Sens. Actuator A: Phys.*, vol. 271, pp. 131–138, 2018.

[38] W. Hu, W. Li, and G. Alici, "3D printed helical soft pneumatic actuators," in *Proc. IEEE/ASME Int. Conf. Adv. Intell. Mechatronics*, 2018, pp. 950–955.

[39] G. Gu, D. Wang, L. Ge, and X. Zhu, "Analytical modeling and design of generalized pneu-net soft actuators with three-dimensional deformations," *Soft Robot.*, vol. 8, no. 4, pp. 462–477, 2021.

[40] D. Wang et al., "Effect of temperature on the programmable helical deformation of a reconfigurable anisotropic soft actuator," *Int. J. Solids Struct.*, vol. 199, pp. 169–180, 2020.

[41] J. Santoso, E. H. Skorina, M. Salerno, S. de Rivaz, J. Paik, and C. D. Onal, "Single chamber multiple degree-of-freedom soft pneumatic actuator enabled by adjustable stiffness layers," *Smart Mater. Struct.*, vol. 28, no. 3, 2019, Art. no. 035012.

[42] A. Tonazzini, S. Mintchev, B. Schubert, B. Mazzolai, J. Shintake, and D. Floreano, "Variable stiffness fiber with self-healing capability," *Adv. Mater.*, vol. 28, no. 46, pp. 10142–10148, 2016.

[43] W. Wang, C. Li, M. Cho, and S. H. Ahn, "Soft tendril-inspired grippers: Shape morphing of programmable polymer-paper bilayer composites," *ACS Appl. Mater. Interfaces*, vol. 10, no. 12, pp. 10419–10427, 2018.

[44] S. Akbari, A. H. Sakhaei, S. Panjwani, K. Kowsari, A. Serjourei, and Q. Ge, "Multimaterial 3D printed soft actuators powered by shape memory alloy wires," *Sens. Actuator A: Phys.*, vol. 290, pp. 177–189, 2019.

[45] K. T. Yoshida, X. Ren, L. H. Blumenschein, A. M. Okamura, and M. Luo, "AFREEs: Active fiber reinforced elastomeric enclosures," in *Proc. 3rd IEEE Int. Conf. Soft Robot.*, 2020, pp. 305–311.

[46] S. Y. Kim, R. Baines, J. Booth, N. Vasios, K. Bertoldi, and R. Kramer-Bottiglio, "Reconfigurable soft body trajectories using unidirectionally stretchable composite laminae," *Nature Commun.*, vol. 10, no. 1, 2019, Art. no. 3464.

[47] J. N. Reddy, *Mechanics of Laminated Composite Plates and Shells: Theory and Analysis*. Boca Raton, FL, USA: CRC Press, 2003.

[48] Z. Chen, C. Majidi, D. J. Srolovitz, and M. Haataja, "Tunable helical ribbons," *Appl. Phys. Lett.*, vol. 98, no. 1, 2011, Art. no. 011906.

[49] W. Flügge, *Tensor Analysis and Continuum Mechanics*. Berlin, Germany: Springer, 1972.

[50] S. G. Lekhnitskii, *Theory of Elasticity of an Anisotropic Body*. Moscow, Russia: Mir Publishers, 1981.

[51] W. S. Slaughter, *The Linearized Theory of Elasticity*. Boston, MA, USA: Birkhäuser, 2002.

[52] Silicone rubber—Platinum cure data sheet, Dec. 2021. [Online]. Available: http://www.smooth-on.com.cn/support/guides/charts/

[53] M. H. Sadd, *Elasticity: Theory, Applications, and Numerics*. Burlington, MA, USA: Academic, 2009.

[54] F. Beer, E. Johnston, J. DeWolf, and D. Mazurek, *Mechanics of Materials*, 7th ed. New York, NY, USA: McGraw-Hill, 2015.

Pei Jiang (Member, IEEE) received the B.S. and Ph.D. degrees in control science and engineering from Zhejiang University, Hangzhou, China, in 2008 and 2015, respectively.

In 2016, he visited the University of Hong Kong for six months. He is currently an Associate Professor with the College of Mechanical and Vehicle Engineering, Chongqing University, Chongqing, China. His research interests include robotic systems, soft robotics, and energy modeling of industrial robots.

Ji Luo received the B.S. degree in mechatronics engineering from East China Jiaotong University, Nanchang, China, in 2020. He is currently working toward the M.S. degree in mechanical engineering with Chongqing University, Chongqing, China.

His research interests include design and modeling of soft robotics.

Jiaxing Li received the B.S. degree from the Qingdao University of Technology, Qingdao, China, in 2017, and the M.S. degree from Chongqing University, Chongqing, China, in 2021, both in mechanical engineering.

He is currently a Software Engineer with TD Technology Co. Ltd., Chengdu, China.

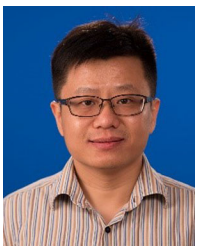

Michael Z. Q. Chen (Senior Member, IEEE) received the B.Eng. degree in electrical and electronic engineering from Nanyang Technological University, Singapore, in 2003, and the Ph.D. degree in control engineering from the University of Cambridge, Cambridge, U.K., in 2007.

He is currently a Professor with the School of Automation, Nanjing University of Science and Technology, Nanjing, China.

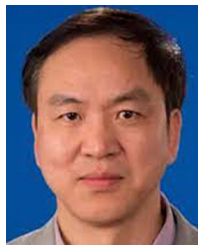

Yonghua Chen (Member, IEEE) received the Ph.D. degree in mechanical engineering from the University of Liverpool, Liverpool, U.K., in 1991.

He is currently an Associate Professor with the Department of Mechanical Engineering, The University of Hong Kong, Pokfulam, Hong Kong. He had worked in industries for three years as a senior R&D engineer. Since 1997, he has organized more than ten international conferences on product development, manufacturing, and robotics. He has also published widely on additive manufacturing (3-D printing and 4-D printing) and soft robotics. He was among the top 1% highly cited researcher in 2021 ranked by Clarivate Analytics.

Dr. Chen had served as an Editorial Board Member for a number of international journals such as *Biofabrication*, *Bio-Design and Manufacturing*, *Journal of Virtual and Physical Prototyping*, and *The RPD Magazine*.

Yang Yang (Member, IEEE) received the B.S. degree in mechanical design manufacturing and automation and the M.S. degree in mechatronics engineering from the Harbin Institute of Technology, Harbin, China, in 2011 and 2013, respectively, and the Ph.D. degree in mechanical engineering from the University of Hong Kong, Hong Kong, in 2017.

He was a Postdoctoral Fellow with both the University of Hong Kong and the Hong Kong University of Science and Technology, Hong Kong, from 2017 to 2020. He is currently an Associate Professor with the Nanjing University of Information Science and Technology, Nanjing. He is also the Vice-Director of the Jiangsu Province Engineering Research Center of Intelligent Meteorological Exploration Robot. His research interests include soft robots, bioinspired robots, 3-D printing, and smart materials.

Rui Chen received the B.S. and Ph.D. degrees in mechanical engineering from Beihang University, Beijing, China, in 2009 and 2014, respectively.

He is currently a Professor with the College of Mechanical and Vehicle Engineering, Chongqing University, Chongqing, China. His current research interests include soft robots and bioinspired robots.